

# Investigation of the effect of low-temperature annealing and impact angle on the erosion performance of nickel-tungsten carbide cold spray coating using design of experiments

Marios Kazasidis<sup>a\*</sup>, Elisa Verna<sup>b</sup>, Shuo Yin<sup>a</sup>, Rocco Lupoi<sup>a\*\*</sup>

<sup>a</sup> Trinity College Dublin, The University of Dublin, Department of Mechanical and Manufacturing Engineering, Parsons Building, Dublin 2, Ireland

<sup>b</sup> Politecnico di Torino, Department of Management and Production Engineering, Corso Duca degli Abruzzi 24, 10129 Torino, Italy

This study investigates the solid particle erosion performance of cold sprayed tungsten carbide-nickel coatings using alumina particles as erodent material. After the coatings fabrication, specimens were annealed in an electric furnace at a temperature of 600 °C for 1 hour. The coatings were examined in terms of microhardness and microstructure in the as-sprayed (AS) and annealed (AN) conditions. Subsequently, the erosion tests were carried out using a General Full Factorial Design with two control factors and two replicates for each experimental run. The effect of the annealing on the erosion behavior of the coating was investigated at the two levels (AS and AN conditions), along with the impact angle of the erodents at three levels (30°, 60°, 90°). Finally, two regression models that relate the impact angle to the mass loss were separately obtained for the two cold spray coatings.

## 1 Introduction

Solid Particle Erosion (SPE) or Solid Particle Impingement Erosion (SPIE) is a particular erosion type that occurs when solid particles dragged by fluid means impinge on the surface of pneumatic or hydraulic systems resulting in loss of their mass. Various potential solutions to the problem have been investigated and applied using different approaches such as the modification of the machinery design, the use of filtration systems, or the adjustment of pressure regulators. From the perspective of materials engineering, the alleviation of SPE in metals has been widely encountered with the fabrication of coatings, using methods such as laser cladding[1], plasma spray[2,3], high-velocity oxyfuel[4], and cold spray[5].

Cermets are metal matrix composites (MMC) reinforced with ceramic particles that attain advanced properties such as impact, corrosion, and wear resistance[6,7], along with a good combination of toughness and hardness[8]. The most common metals employed for the fabrication of the matrix are cobalt, nickel, and iron, while alumina, tungsten carbide, silicon carbide, and titanium carbide frequently constitute the secondary particles[6,8–10]. Their use in the protection of metallic materials from SPE has shown promising results[7,11] as their resistance is generally superior to that of their metal matrix[12].

The complex nature of the SPE mechanism involves several variables with the erodent properties (e.g. feed rate, velocity, size, hardness), and the impingement angle to be the predominant ones[5,7,13,14]. Meanwhile, the intrinsic properties of the materials have been reported to inverse the effect of the variables on the erosion resistance. For instance, ductile materials are considered to exhibit better erosion resistance as the impingement angle approaches 90°, while brittle materials at oblique angles (closer to 0°)[7,15]. As a result, the identification of a standard method that predicts the erosion performance of coatings is extremely difficult[14,15]. To this end, one of the most widely adopted techniques to assess the effect of control variables on coating erosion resistance is the Design of Experiments (DOE)[16]. Studies over the past years have provided new insights on the understanding of experimental results, using DOE methodology. More specifically, the erosion resistance has been investigated in coatings produced through thermal spray technologies such as high-velocity oxyfuel[13,17], plasma spray[18], arc ion plating[19], and filtered cathodic vacuum arc technique[20]. Nevertheless, few empirical studies have investigated the erosion performance of cold spray coatings through experimental design[21], which is a major innovative aspect of the present publication.

The authors adopted a General Full Factorial Design (GFFD) to scrutinize the solid particle erosion resistance of the cold sprayed nickel-tungsten carbide coating produced with a WC/Ni composite powder. GFFD with factors varying on multiple levels is widely recognized as a more appropriate method than other experimental designs for modelling complex multivariate systems due to its application flexibility[16,22–24]. Nickel was qualified over cobalt to constitute the binder phase as it is considered to attain better corrosion and oxidation resistance, particularly at elevated temperatures[1,6]. Moreover, tungsten carbide was selected as the reinforcement material due to its high density, hardness, and melting point which improve the erosion resistance[7], while it is eligible for heat treatment[25]. The cold spray technique was employed for the coating fabrication to prevent metallurgical phenomena such as the decarburization of WC[9,26], and the formation of undesirable phases such as W<sub>2</sub>C, W, and eta (η) phase[26,27].

---

\* Corresponding author: marios\_kazasidis@hotmail.com

\*\* Corresponding author: lupoi@tcd.ie

The coatings were deposited on the substrate and subsequently characterized in terms of microstructure. Regarding the erosion process, the parameters under investigation used as factors of the experimental plan were the impingement angle (angle between the erodent velocity and the coating surface) and the coating condition (as-sprayed and annealed). The loss of mass was the main output response of the problem, while the statistical significance of the effect of control factors on the erosion performance was estimated using the Analysis of Variance (ANOVA). The diagnostic checking tests, such as the coefficients of determination and the residual plots, were used to interpret the results of the factorial design. Then, two regression models relating the impact angle and the mass loss were obtained separately for the two coating conditions. Finally, the obtained regression models were optimized to identify the optimum, namely the set of control factors that lead to the minimum mass loss.

## 2. Experimental part

### 2.1 Materials and cold spray process

The feedstock powder of the cold spray process consisted of Ni (-45/+16  $\mu\text{m}$ , Praxair), and WC/Ni (-45/+15  $\mu\text{m}$ , Flame Spray Technologies) powders, mechanically mixed at a 1:4.5 mass ratio. The powders were fed into a custom-made cold spray system (Trinity College Dublin, Ireland) through a powder hopper (PF100WL, Uniquocoat Technologies LLC, USA), with a rate of 80 g/min, and subsequently sprayed on the as-machined surface of 4 mm thick stainless steel plates.

Nitrogen was used as propellant gas at a pressure of 3.0 MPa and a preheating temperature of 850 °C. The particles were accelerated towards the substrate through a WC-Co De Laval nozzle with a divergent length of 190 mm, throat diameter of 3 mm, and outlet diameter of 8 mm. Its standoff distance and transversal velocity during the spraying process were set at 40 mm and 25 mm/s, respectively. The selected building strategy followed a zig-zag pattern in two passes and resulted in a coating thickness of approximately 1.4 mm.

### 2.2 Materials characterization

Specimens extracted from coatings as well as feedstock powders were mounted into a conductive resin to be subjected to standard metallographic techniques for microstructure observation. The etching was selectively carried out using Kalling's reagent. The cross-sections of the mounted samples were subsequently observed with an optical microscope and a Scanning Electron Microscope (SEM, Carl Zeiss UTRA, CRANN). The calculation of the average porosity and WC retention in the coatings was performed with Image J analysis software analyzing five optical micrographs of specimens in both states. For the assessment of the annealing effect on the coating properties, their microhardness in the as-sprayed and the annealed conditions was estimated after ten repetitions, using a Vickers microhardness tester (Mitutoyo MVK-H1, Japan).

### 2.3 Annealing and Erosion testing

A General Full Factorial Design (GFFD) was adopted for the execution of the SPE tests. In this paper, the selected control factors were the impact angle ( $a$ ) and the condition of the coating (C), i.e. as-sprayed (AS) and annealed (AN).

Rectangular specimens with dimensions 45x25 mm<sup>2</sup> were extracted from the cold sprayed plates and milled on the top surface. Six of the specimens were annealed in a vacuum furnace at 600 °C for 1 h, using a ramp rate of 10 °C/min and a slow cooling at the end of the process. Another six specimens remained in the as-sprayed condition. The levels of the control factors used in the GFFD are listed in Table 1.

**Table 1. The control factors' levels used in the planned experimentation.**

| Control factors          | Levels       |
|--------------------------|--------------|
| Impact angle ( $a$ ) [°] | 30 - 60 - 90 |
| Condition of coating (C) | AS - AN      |

In total, twelve (12) erosion tests were executed, as the design was replicated twice to improve the accuracy of the predicted results. The experiments were randomized, as shown in Table 1.

**Table 1. General Full Factorial Design (GFFD) table of the SPE tests.**

| Run order | 1  | 2  | 3  | 4  | 5  | 6  | 7  | 8  | 9  | 10 | 11 | 12 |
|-----------|----|----|----|----|----|----|----|----|----|----|----|----|
| $a$ [°]   | 90 | 90 | 30 | 60 | 30 | 60 | 60 | 30 | 90 | 90 | 60 | 30 |
| C         | AN | AS | AS | AS | AN | AS | AN | AS | AS | AN | AN | AN |

The experimental set-up of the SPE test is illustrated in Figure 1. The particles of the alumina erodents attained a nominal size of 90  $\mu\text{m}$ . They were supplied into the system through a hopper, subsequently dragged by com-

pressed air at 3.0 bar, and ejected axially through the nozzle. The cold sprayed specimens were placed into the sample holder of adjustable angle and a standoff distance of 20 mm. The duration of each SPE test was 10 min.

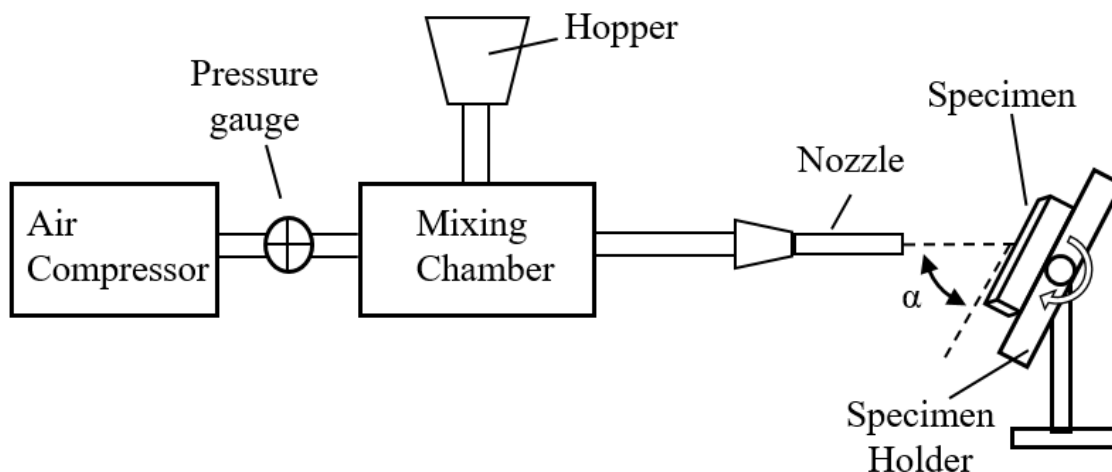


Figure 1. The experimental set up of the solid particle erosion testing.

### 3. Results and Discussion

#### 3.1 Powders characterization

The composite agglomerated and sintered powder (**Error! Reference source not found.a**) consisted of nanostructured tungsten carbide particles embedded into a porous nickel matrix which facilitated their deposition on the final coating[28]. Ni powder (**Error! Reference source not found.b**) attained spherical morphology with some dispersed agglomerations, while alumina particles attained angular shape (**Error! Reference source not found.c**). As can be observed in the inserts of Figures 2a and b, the composite and nickel powders have porous and compact cross-sections respectively, resulting from their processing method.

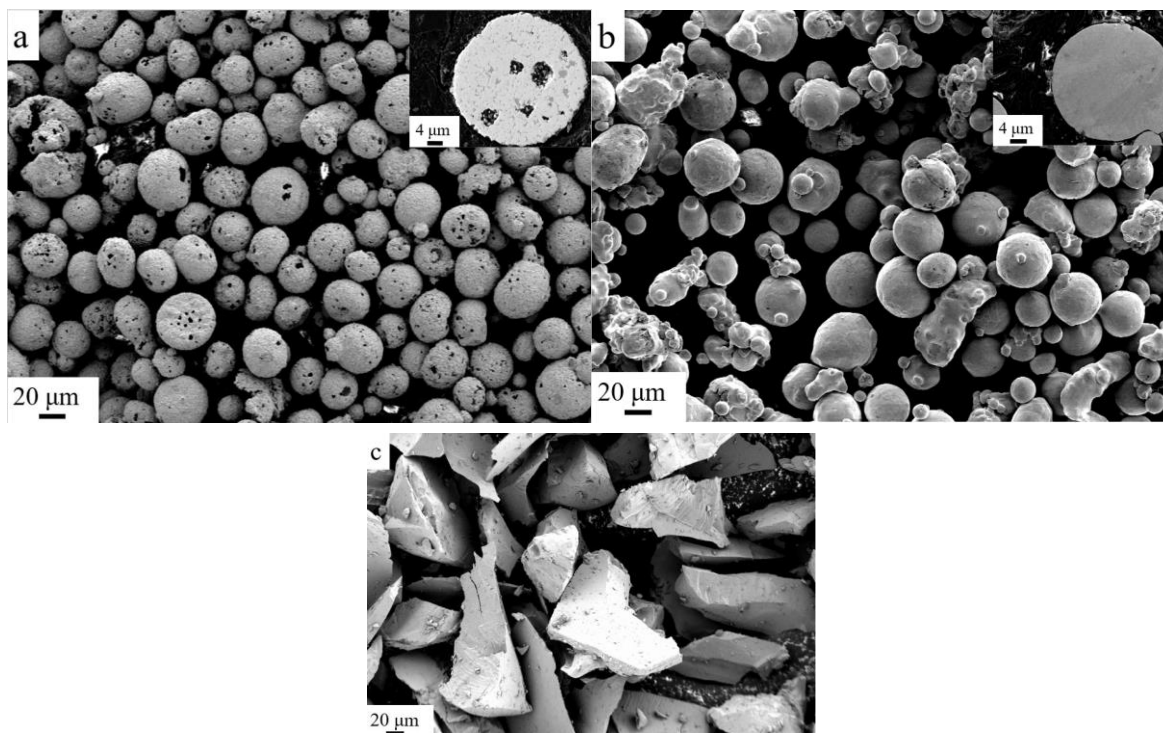
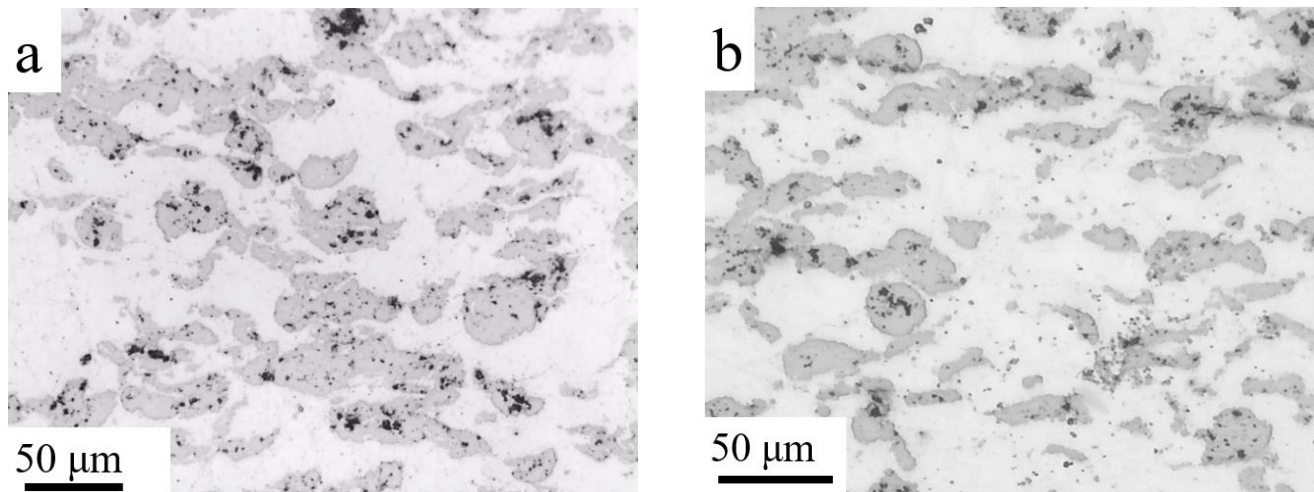


Figure 2. Electron micrographs of the feedstock powders, a) composite WC/Ni powder, b) Nickel powder, c) alumina erodent particles.

### 3.2 Microstructural characterization of the coatings

The as-polished surfaces of the cold sprayed coatings in the as-sprayed and annealed conditions are indicatively presented in **Error! Reference source not found.a** and **b**.



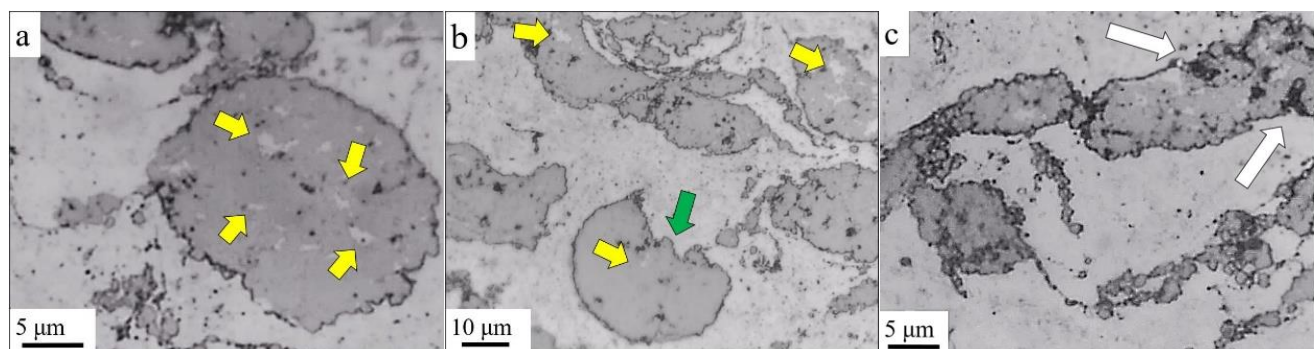
**Figure 3.** Optical micrographs of the as polished cold sprayed composite coatings in a) as-sprayed, and b) annealed conditions.

The distinct areas of the coating, i.e. carbide particles, nickel matrix, and pores, attained grey, white and black color, respectively. Concerning the tungsten carbide recovery in the cold spray coatings, it was almost equal for the as-sprayed and annealed coatings, as expected. Their respective percentages were measured at  $42.8 \pm 3.7$  vol.% (AS) and  $40.1 \pm 1.1$  vol.% (AN).

The porosity of the cold sprayed coatings was found to be  $5.2 \pm 1.6$  vol.% and  $1.8 \pm 0.8$  vol.% for the as-sprayed and annealed conditions, respectively. This significant difference indicates that the selected annealing strategy contributed to the reduction of the cold sprayed coating porosity, leading to an ample densification of the coating that resulted from the atomic diffusion and mass rearrangement across the inter-particle interfaces.

This beneficial effect of the heat treatment on the porosity level was also highlighted by Tang et al.[29], who also reported a decrease from above 1.7% to below 0.5% when annealed Ti-WC cermet at 650 °C for 1h and argon atmosphere. On the contrary, Sun et al.[30] reported an unaltered porosity level of Inconel 718 cold sprayed coatings after furnace heat treatment in vacuum at 900 °C for 10 min. Similarly, Wong et al.[31] reported that annealing for 2 h under shielding atmosphere at temperatures of 950 °C, 1010 °C, and 1060 °C did not result in differentiation of porosity in the case of Inconel 718 cold sprayed coatings. Based on the aforementioned publications and the results obtained in this study, it can be stated that the annealing effect on the porosity depends mainly on the type of the material, the heat treatment method, the holding temperature, and the holding time.

After etching, the contours of the nickel and tungsten carbide particles became more prominent, as shown in **Error! Reference source not found..** The composite nickel-tungsten carbide powder can consolidate in the coatings as intact (**Error! Reference source not found.a**), partially fractured (**Error! Reference source not found.b**, green arrow), and entirely fractured (Figure 4c, e) particles that may attain a necklace-like structure (**Error! Reference source not found.d**, white arrow). In the first two cases, dispersed nickel islands can be found surrounded by the tungsten carbide agglomerations, as indicated by the yellow arrows in **Error! Reference source not found.a** and **b**. The WC particles cannot undergo plastic deformation, which is the main mechanism of porosity elimination. As a result, the brittle fracture of some carbides leads to the inhomogeneous pores distribution into the coating and their accumulation along the vicinity or the interior of tungsten carbide clusters (white arrows in **Error! Reference source not found.c**, 4f).



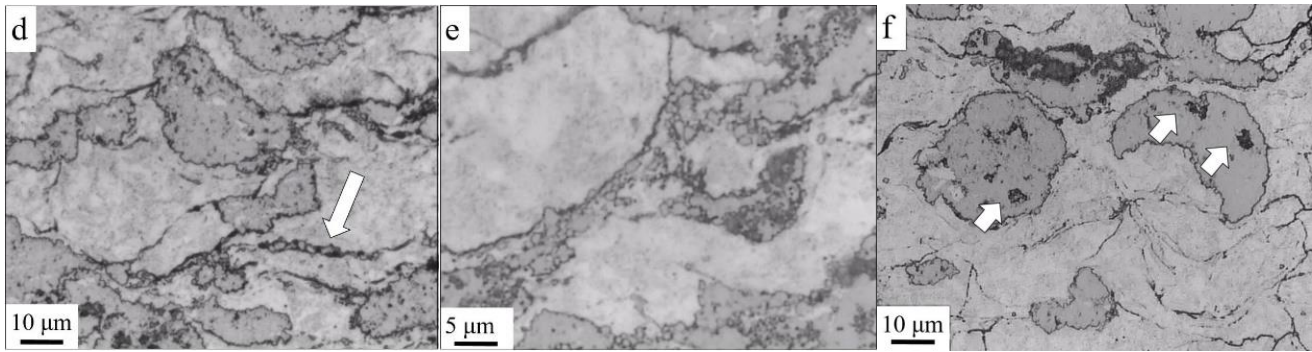


**Figure 4.** Optical micrographs of the etched cold sprayed composite coatings in a), b), c) as-sprayed, and d), e) f) annealed conditions.

The microhardness values (see Figure 5) of the coatings were estimated at  $335\pm 68$  and  $226\pm 34$  HV0.3 for the as-sprayed and the annealed conditions, respectively. Therefore, it can be stated that the selected annealing strategy led to a decrease of 32% of the coating microhardness as well as to its homogenization, as indicated by the substantially lower standard deviation.

The recrystallization temperature ( $T_r$ ) of pure nickel (99.99 wt.%) is approximately 370 °C while it additionally depends on the holding time above the critical temperature as well as the amount of impurities[32]. In the case of cold sprayed coatings, the high level of work hardening due to the cold spray process further lowered the  $T_r$ [33], which lies below the selected holding temperature of the current study (600 °C). As a result, partial or entire recrystallization of the nickel matrix should be considered as the main factor that contributed to the reduction of the hardness value of the annealed coating.

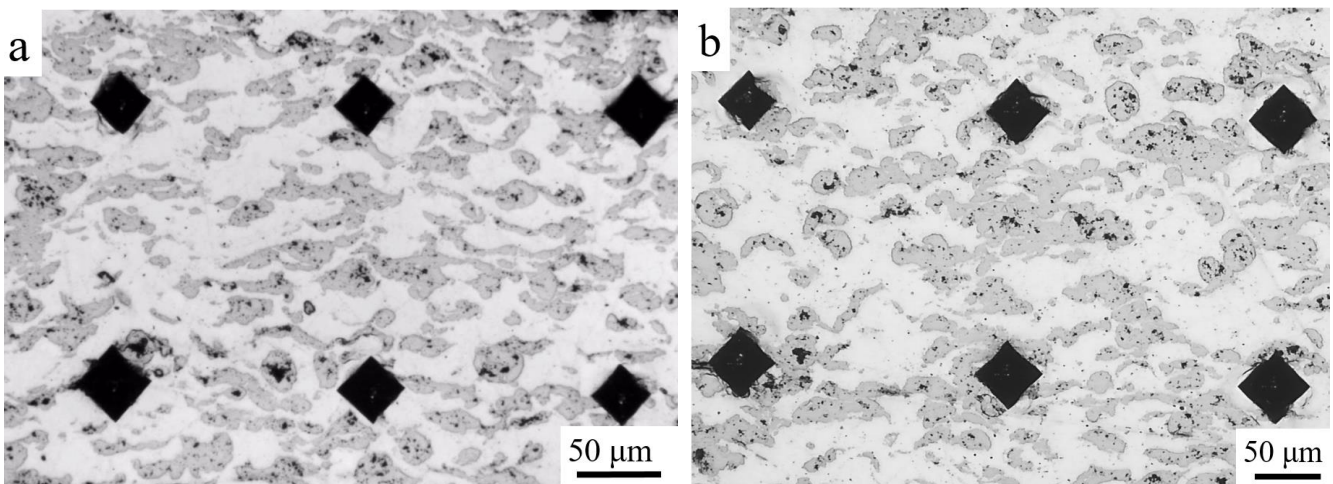


**Figure 5.** Microhardness indentations as obtained with the Vickers method: a) as-sprayed coating, b) annealed coating.

### 3.3 Solid particle impingement erosion test

#### 3.3.1 Analysis of GFFD

After the end of the erosion experiments, the accumulative mass loss was used as the response to evaluate the coatings' erosion performance. The aggregated results, which are summarized in Table 2, were statistically analyzed using the software MINITAB®.

**Table 2. Mass loss results of the GFFD for the SPE tests after 10 min.**

| Run order     | 1     | 2     | 3     | 4     | 5     | 6     | 7     | 8     | 9     | 10    | 11    | 12    |
|---------------|-------|-------|-------|-------|-------|-------|-------|-------|-------|-------|-------|-------|
| a [°]         | 90    | 90    | 30    | 60    | 30    | 60    | 60    | 30    | 90    | 90    | 60    | 30    |
| C             | AN    | AS    | AS    | AS    | AN    | AS    | AN    | AS    | AS    | AN    | AN    | AN    |
| Mass loss (g) | 0.153 | 0.184 | 0.340 | 0.198 | 0.284 | 0.206 | 0.196 | 0.335 | 0.171 | 0.148 | 0.223 | 0.271 |

The ANOVA table is shown in Table 3, while the main effect and the interaction plots are given in **Error! Reference source not found.**. As shown in **Error! Reference source not found.a**, the angle is the most significant factor that affects the mass loss. Angles of 90°, 60°, and 30° produce an average mass loss of about 0.16 g, 0.21 g, and 0.3 g, respectively. Regarding the coating condition, when as-sprayed, the coating is characterized by an average mass loss of 0.24 g, which decreases to 0.21 g in the annealed condition (**Error! Reference source not found.a**). At 30° and 90°, the mass loss is higher when the coating is as-sprayed, while at 60°, it is slightly lower (Figure 6b). In qualitative terms, the interaction between the two variables is presented in **Error! Reference source not found.b** where they indicate a degree of interaction, as their lines diverge from the parallel state[16]. These results were also confirmed using the ANOVA where the angle, the coating state, and their interaction were found to be highly significant since the corresponding p-values were less than 1%.

**Table 3. Analysis of variance (ANOVA) for mass loss (g), with the indication of the source of variation, degrees of freedom (DF), Adjusted sum of squares (Adj SS), F-value, and p-value<sup>[34]</sup>.**

| Source    | DF | Adj SS   | F-Value | p-Value |
|-----------|----|----------|---------|---------|
| a [°]     | 2  | 0.042809 | 222.83  | 0.000   |
| C         | 1  | 0.001984 | 20.66   | 0.004   |
| a [°] * C | 2  | 0.002154 | 11.21   | 0.009   |
| Error     | 6  | 0.000576 | -       | -       |
| Total     | 11 | 0.047523 | -       | -       |

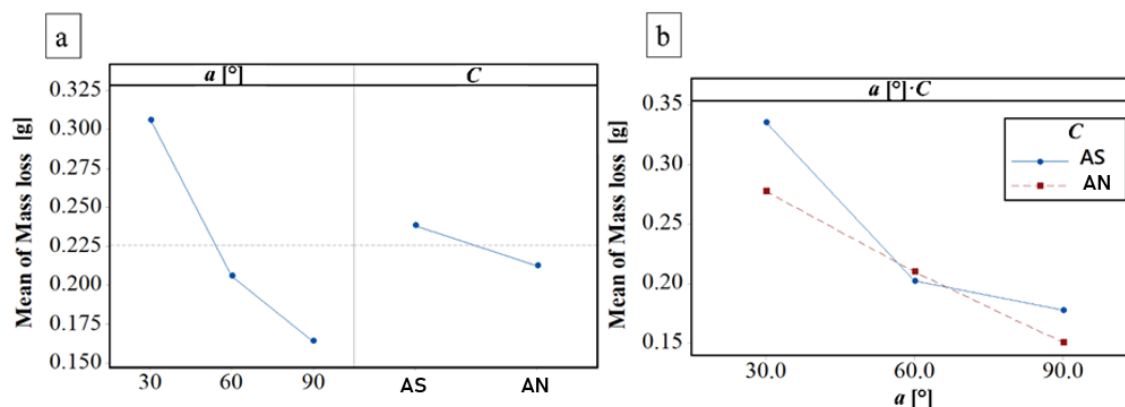


**Figure 6** a) Main effect plot and, b) interaction plot for mass loss.

The two variables and their interaction were used to develop two regression models to obtain a relationship with the mass loss and predict the erosion performance of future tests. The obtained regression models are reported in Eqs. (1) and (2) for the AS and AN conditions, respectively.

$$C = AS \quad \text{Mass loss (g)} = 0.3961 - 0.002631 a \text{ (}^\circ\text{)} \quad (1)$$

$$C = AN \quad \text{Mass loss (g)} = 0.3394 - 0.002115 a \text{ (}^\circ\text{)} \quad (2)$$

The residual analysis for the model was performed, both from a graphical and a quantitative point of view by plotting the residual plots and by performing the Anderson–Darling test, showing that the residuals follow a normal distribution. The coefficient of determination<sup>[35]</sup> ( $R^2$ ), which is a goodness of fit measure of the model, reveals that the observed variation in the mass loss explained by the model is 98.79%. Also, the predicted  $R^2$  is very high, reaching 95.15%.

From the optimization of the regression curves, the combination of the variables that minimizes the mass loss was obtained. These setups are summarized in Table 4, together with the predicted values.

**Table 4. Variables setup that minimizes mass loss, predicted mass loss and corresponding 95% confidence interval.**

| Variables setup |    | Mass loss prediction (g) |                         |
|-----------------|----|--------------------------|-------------------------|
| a (°)           | C  | Predicted mass loss      | 95% confidence interval |
| 90              | AN | 0.15                     | (0.12; 0.18)            |

It is interesting to observe that although the best combination of variables is an angle of 90° and the AN condition, annealing is particularly beneficial at 30°. On average, annealing reduced the mass loss compared to the as-sprayed condition by almost 20%. On the contrary, at higher angles (60° and 90°), the difference between the AS

and AN conditions is not so pronounced and is less statistically significant by performing the two-sample t-test<sup>[35]</sup> compared to 30° angle.

Moreover, as stated by Buszko et al.[36], there may be significant interaction of the alumina particles that approach the eroded surface with those that rebound from it, while this phenomenon is higher as the erodent velocity tends to be normal to the plane of the coating surface, and therefore the respective impact angle is closer to 90°<sup>[37]</sup>. This could be a factor that contributed to the general trend of the erosion rate decline with increasing the impact angle of the alumina particles (**Error! Reference source not found.**).

### 3.3.2 Analysis of the eroded areas

The macrophotographs of the eroded surfaces are depicted in Figure 7. All marks consist of a deep central zone where the primary erosion damage occurred, and the halo regions of the secondary zone, where the particle impact events were significantly fewer and resulted in surface roughening. The shape of the erosion scar is elliptical at the low impact angle of 30° and tends to become circular when the impact angle reaches 90°. It can be observed that the annealing did not induce any significant variation in the surface area or the shape of the erosion marks.

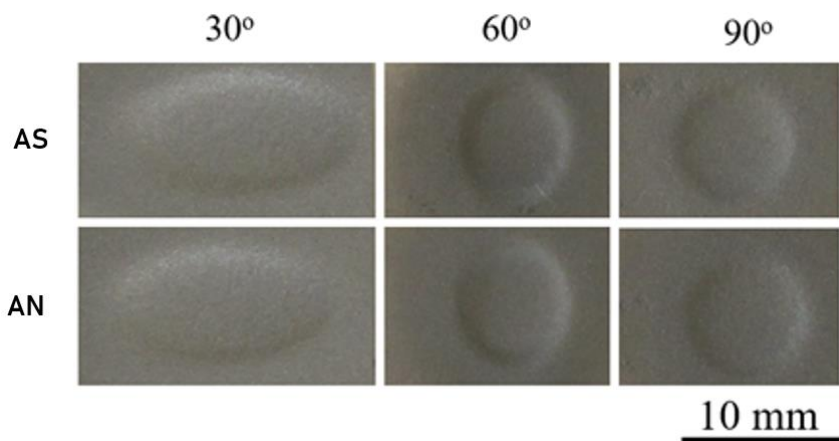


**Figure 7.** The obtained imprints after 10 min of solid particle impingement erosion with alumina particles.

The erosion angle affected not only the shape of the erosion marks but also their surface area that was found to decrease with increasing the impact angle. This can be a major reason that contributed to the higher erosion rates at low impact angles.

Figure 8 depicts indicative electron micrographs taken inside the eroded area after the erosion tests. In general, the coatings demonstrated different erosion characteristics in WC enriched or depleted areas. As expected, tungsten carbide rich areas were found to be more resistant to scooping as their well-consolidated particles shield the underlying matrix. Moreover, no significant differences in the erosion characteristics were observed between the as-sprayed and annealed conditions. However, in the latter case, the erosion attains more ductile characteristics (Figure 8d, e, f), which is consistent with its lower hardness after the annealing process. At the low impingement angle (30°), where the erosion rate is higher, ploughing is a major mechanism of material removal. Alumina particles slide while scratching the nickel matrix (Figures 8a, d). Areas with a high percentage of tungsten carbides tend to deform under the repetitive impact of the erodent particles while creating irregular erosion morphology characterized by concavities and protrusions. Figure 8d presents such a case where the coating shows significant surface retention of the carbides. At an impact angle of 60°, the coatings exhibit grooves and craters along with striations formed on nickel particles (Figure 8b). At an impact angle of 90°, irregular smeared indentations appear on the coating erosion surface and striations on a consolidated alumina particle, while the impact of the alumina may flatten the nickel matrix locally (Figure 8c). In addition, the cavities become deeper and sharper, especially in the more ductile annealed coating (Figure 8f).

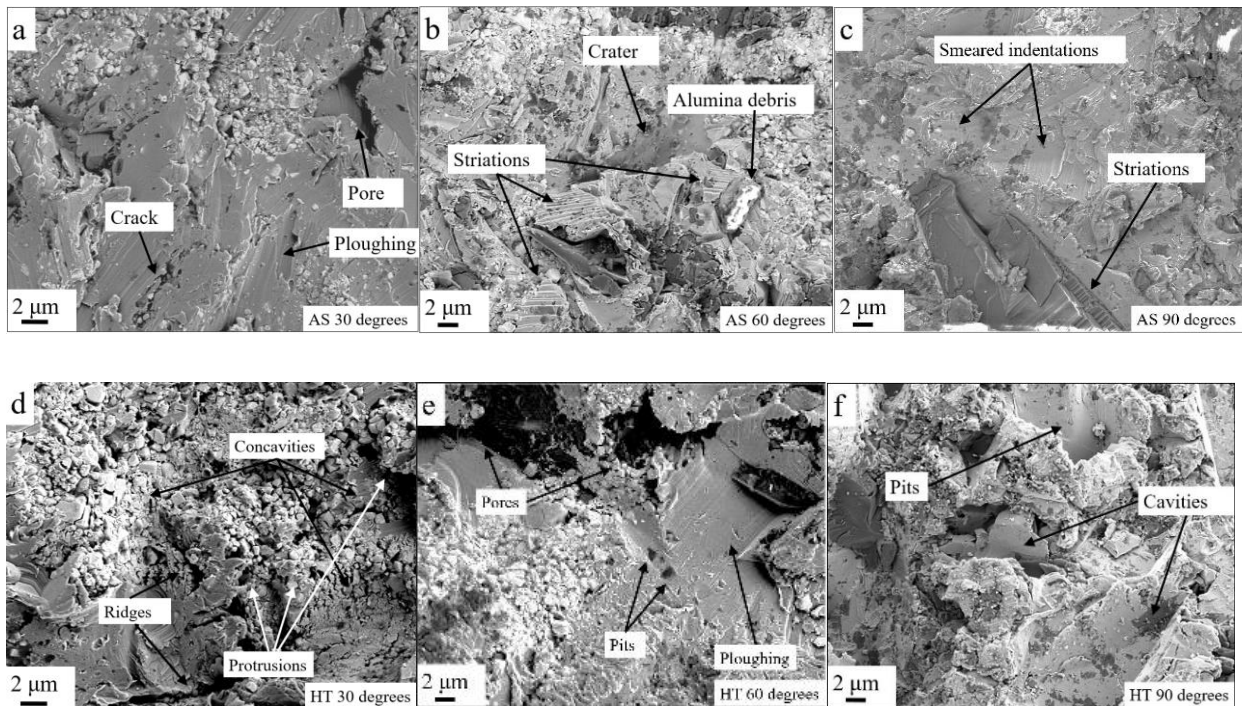


**Figure 8.** SEM images of the eroded areas of the WC/Ni coatings: a) AS-30 degrees, b) AS-60 degrees, c) AS-90 degrees, d) AN-30 degrees, e) AN-60 degrees, f) AN-90 degrees.

#### 4 Conclusions

The authors investigated the microstructure and the solid particle erosion performance of nickel cold sprayed coatings, focusing on the effect of the impact angle and the annealing on it. The major conclusions that can be drawn are summarized as follows:

- The tungsten carbide retention in the final coating was in the order of 41 vol.%, following a reduction of 40% compared to the feedstock powder.
- Annealing under vacuum conditions resulted in a significant reduction of the hardness, while it seems to mitigate the porosity.
- Among the two factors that were investigated (impact angle and coating condition), the impact angle of the erodents was found to affect to a greater extent the mass loss of the coating.
- The effect of impact angle and coating condition, as well as their interaction, were found to be statistically significant with respect to the mass loss.
- Two regression models were built for prevision and optimization purposes, separately for as-sprayed and annealed conditions, relating impact angle and mass loss.
- It was found that the mass loss is minimized using an angle of 90° and a coating annealed at 600 °C.

#### Acknowledgments

The authors would like to thank Enterprise Ireland (EI) and SchuF Valve Technology GmbH (IP2018 0730) for their financial support.

#### Literature

- [1] Paul CP, Mishra SK, Tiwari P, Kukreja LM. Solid-Particle Erosion Behaviour of WC/Ni Composite Clad layers with Different Contents of WC Particles. *Opt Laser Technol* 2013;50:155–62. <https://doi.org/10.1016/j.optlastec.2013.03.002>.
- [2] Swain B, Swadhin P, Priyabrata M, Mohapatra S, Behera A. Solid particle erosion wear of plasma sprayed NiTi alloy used for aerospace applications. *ITSC, Proc. Int. Therm. Spray Conf.*, Yokohama: ASM International; 2019.
- [3] Branco JRT, Gansert R, Sampath S, Berndt CC, Herman H. Solid particle erosion of plasma sprayed ceramic coatings. *Mater Res* 2004;7:147–53. <https://doi.org/10.1590/s1516-14392004000100020>.
- [4] Lian Y, Li Y. Investigation on erosion resistance of WC-Co-Cr coatings. *Tribol Online* 2018;13:36–42. <https://doi.org/10.2474/trol.13.36>.
- [5] Alidokht S, Vo P, Yue S, Chromik RR. Erosive wear behavior of Cold-Sprayed Ni-WC composite coating. *Wear* 2017;376–377:566–77. <https://doi.org/10.1016/j.wear.2017.01.052>.
- [6] Hussainova I. Some aspects of solid particle erosion of cermets. *Tribol Int* 2001;34:89–93.



[https://doi.org/10.1016/S0301-679X\(00\)00140-7](https://doi.org/10.1016/S0301-679X(00)00140-7).

- [7] ASM International. ASM Handbook, Volume 18: Friction Lubrication and Wear Technology. ASM International; 2018.
- [8] Fernandez R, Jodoin B. Cold Spray Aluminum–Alumina Cermet Coatings: Effect of Alumina Morphology. *J Therm Spray Technol* 2019;28:737–55. <https://doi.org/10.1007/s11666-019-00845-5>.
- [9] Yin S, Ekoi EJ, Lupton TL, Dowling DP, Lupoi R. Cold spraying of WC-Co-Ni coatings using porous WC-17Co powders: Formation mechanism, microstructure characterization and tribological performance. *Mater Des* 2017;126:305–13. <https://doi.org/10.1016/j.matdes.2017.04.040>.
- [10] Alidokht SA, Manimunda P, Vo P, Yue S, Chromik RR. Cold spray deposition of a Ni-WC composite coating and its dry sliding wear behavior. *Surf Coatings Technol* 2016;308:424–34. <https://doi.org/10.1016/j.surfcoat.2016.09.089>.
- [11] Rateick RG, Karasek KR, Cunningham AJ, Goretta KC, Routbort JL. Solid-particle erosion of tungsten carbide/cobalt cermet and hardened 440C stainless steel-A comparison. *Wear* 2006;261:773–8. <https://doi.org/10.1016/j.wear.2006.01.012>.
- [12] Miyazaki N. Solid particle erosion of composite materials: A critical review. vol. 50. 2016. <https://doi.org/10.1177/0021998315617818>.
- [13] Kiragi VR, Patnaik A, Singh T, Fekete G. Parametric optimization of erosive wear response of TiAlN-coated aluminium alloy using Taguchi method. *J Mater Eng Perform* 2019;28:838–51.
- [14] Sahu S, Satapathy A, Patnaik A, Sreekumar KP, Ananthapadmanabhan P V. Development , characterization and erosion wear response of plasma sprayed fly ash – aluminum coatings. *Mater Des* 2010;31:1165–73. <https://doi.org/10.1016/j.matdes.2009.09.039>.
- [15] Parsi M, Najmi K, Naja F, Hassani S, Mclaury BS, Shirazi SA. *Journal of Natural Gas Science and Engineering A comprehensive review of solid particle erosion modeling for oil and gas wells and pipelines applications* 2014;21:850–73. <https://doi.org/10.1016/j.jngse.2014.10.001>.
- [16] Montgomery DC. *Design and analysis of experiments*. 9th Ed. New York: John Wiley & Sons; 2017.
- [17] Praveen AS, Sarangan J, Suresh S, Channabasappa BH. Optimization and erosion wear response of NiCrSiB/WC–Co HVOF coating using Taguchi method. *Ceram Int* 2016;42:1094–104.
- [18] Sahu SP, Satapathy A, Patnaik A, Sreekumar KP, Ananthapadmanabhan P V. Development, characterization and erosion wear response of plasma sprayed fly ash–aluminum coatings. *Mater Des* 2010;31:1165–73.
- [19] Wang D, Lin S, Liu L, Yang H, Shi J, Jiang B, et al. Micro-nano multilayer structure design and solid particle erosion resistance performance of CrAlN<sub>x</sub>/CrAlN coating. *Vacuum* 2020;172:109064.
- [20] Cao X, He W, Liao B, Zhou H, Zhang H, Tan C, et al. Sand particle erosion resistance of the multilayer gradient TiN/Ti coatings on Ti6Al4V alloy. *Surf Coatings Technol* 2019;365:214–21.
- [21] Hu HX, Jiang SL, Tao YS, Xiong TY, Zheng YG. Cavitation erosion and jet impingement erosion mechanism of cold sprayed Ni-Al<sub>2</sub>O<sub>3</sub> coating. *Nucl Eng Des* 2011;241:4929–37. <https://doi.org/10.1016/j.nucengdes.2011.09.038>.
- [22] Rafidah A, Nurulhuda A, Azrina A, Suhaila Y, Anwar IS, Syafiq RA. Comparison design of experiment (doe): Taguchi method and full factorial design in surface roughness. *Appl. Mech. Mater.*, vol. 660, Trans Tech Publ; 2014, p. 275–9.
- [23] Das D, Dwivedi A. Parametric optimization of heat transfer from triangular fin array within a rectangular enclosure using design of experiment (DOE): a comparative analysis. *J Inst Eng Ser C* 2013;94:335–43.
- [24] Verna E, Biagi R, Kazasidis M, Galetto M, Bemporad E, Lupoi R. Modeling of erosion response of cold-sprayed In718-Ni composite coating using full factorial design. *Coatings* 2020;10. <https://doi.org/10.3390/coatings10040335>.
- [25] Zhongnan X, Li Z, Fa C, Pinqiang D. Effect of Heat Treatment on the Microstructure and Properties of Ultrafine WC–Co Cemented Carbide 2019:1–12.
- [26] El Rayes MM, Abdo HS, Khalil KA. Erosion - Corrosion of cermet coating. *Int J Electrochem Sci* 2013;8:1117–37.
- [27] Couto M, Dosta S, Torrell M, Fernández J, Guilemany JM. Cold spray deposition of WC-17 and 12Co cermets onto aluminum. *Surf Coatings Technol* 2013;235:54–61. <https://doi.org/10.1016/j.surfcoat.2013.07.011>.
- [28] Alidokht SA, Lengaigne J, Klemberg-Sapieha JE, Yue S, Chromik RR. Effect of Microstructure and Properties of Ni-WC Composite Coatings on Their Solid Particle Erosion Behavior. *J Mater Eng Perform* 2019;28:1532–43. <https://doi.org/10.1007/s11665-019-03956-w>.
- [29] Tang J, Saha GC, Richter P, Kondás J, Colella A, Matteazzi P. Effects of Post-spray Heat Treatment on Hardness and Wear Properties of Ti-WC High-Pressure Cold Spray Coatings. *J Therm Spray Technol* 2018;27:1153–64. <https://doi.org/10.1007/s11666-018-0762-7>.
- [30] Sun W, Bhowmik A, Tan AWY, Li R, Xue F, Marinescu I, et al. Improving microstructural and mechanical characteristics of cold-sprayed Inconel 718 deposits via local induction heat treatment. *J Alloys Compd* 2019;797:1268–79. <https://doi.org/10.1016/j.jallcom.2019.05.099>.
- [31] Wong W, Irissou E, Vo P, Sone M, Bernier F, Legoux JG, et al. Cold spray forming of Inconel 718. *J Therm Spray Technol* 2013;22:413–21. <https://doi.org/10.1007/s11666-012-9827-1>.

- [32] Mitchell BS. Materials Engineering and Science an Introduction To Materials Engineering and Science for Chemical and Materials Engineers. 2014.
- [33] Bhaduri A. Mechanical Properties and Working of Metals and Alloys. 2003. <https://doi.org/10.1016/B978-075067509-3/50025-7>.
- [34] Montgomery DC, Runger GC, Hubele NF. Engineering statistics. Hoboken, NJ, USA: 20011.
- [35] Devore JL. Probability and Statistics for Engineering and the Sciences. Boston, USA: Cengage learning; 2011.
- [36] Buszko MH, Krella AK. An Influence of Factors of Flow Condition, Particle and Material Properties on Slurry Erosion Resistance. *Adv Mater Sci* 2019;19:28–53. <https://doi.org/10.2478/adms-2019-0010>.
- [37] Laguna-Camacho JR, Gallardo-Hernandez EA, Vera-Cardenas EE. Solid Particle Erosion on Different Metallic Materials, *Tribology in Engineering* 2013:63–78. <https://doi.org/10.5772/51176>.